scientific reports

Check for updates

OPEN

Structural and optical properties of $Y_3Al_5O_{12}$ single crystals irradiated by swift heavy Xe ions

Alma Dauletbekova[1]✉, Zhadiger Dosmagambetov[1], Ilze Manika[2], Reinis Ignatans[2], Krisjanis Smits[2], Artur Majewski-Napierkowski[3], Yuriy Zorenko[3], Abdirash Akilbekov[1], Ruslan Assylbayev[4], Anatoli I. Popov[2], Zhakyp Karipbayev[1] & Gulnara Aralbayeva[1]

The multifaceted radiation effects occurring in advanced optical material – the crystals of yttrium aluminum garnet $Y_3Al_5O_{12}$, irradiated by swift heavy 230 MeV Xe ions to fluences of 6×10^{10}-10^{13} ions/cm^2 have been investigated using various research techniques, including optical absorption, Raman spectroscopy, photoluminescence under excitation by the synchrotron radiation, nanohardness measurements, and high-resolution transmission electron microscopy. The near-surface layer at high fluence becomes amorphous, and material softening indicates destruction of cation-anion bonds due to tracks overlapping. Transmission electron microscopy analysis confirmed the presence of continuous tracks in irradiated $Y_3Al_5O_{12}$ crystals at energy losses above 10 keV/nm, whereas lower-energy tracks appear as chains of smaller defects. The core track diameter is $d_c \approx (5.00 \pm 0.15)$ nm, with a surrounding damaged region of $d_d \approx (10.00 \pm 0.15)$ nm. An increase in the concentration of oxygen vacancies (F and F$^+$ centers) and Y_{Al} antisite defects with increasing irradiation fluence is confirmed through photoluminescence spectra of initial and irradiated crystals at 9 K. In addition, Y_{Al}–F$^+$ and/or Y_{Al}–F dimers may form based on antisite defects associated with F-like centers, as a result of melting and crystalization processes occurring during track formation under Xe ion irradiation.

Keywords $Y_3Al_5O_{12}$, Optical absorption and photoluminescence, Synchrotron radiation, Raman spectra, Nanohardness, Swift heavy ions

Multicomponent wide-gap oxide materials with a garnet structure (see Fig. 1) are valuable advanced materials with a very wide range of applications. A remarkable representative of this class of materials is yttrium aluminium garnet $Y_3Al_5O_{12}$ (YAG)[1–10].

The crystal structure of YAG (cubic space group $Ia\bar{3}d$, lattice parameter approximately 12 Å)[11]. It is well studied and represented by a system of polyhedrons: dodecahedrons, octahedrons, and tetrahedrons. Figure 1a shows the detailed structure of the YAG host. Figures 1a and b also show the polyhedron structure, with separate images of the dodecahedron, octahedron, and tetrahedron in different colors.

Generally, the YAG structure consists of dodecahedrons, where Y^{3+} ions are localized, and octahedrons as well as tetrahedrons, which contain Al^{3+} ions (Fig. 1). This architecture ensures high lattice stability while allowing for extensive opportunities for isomorphous substitution, which makes YAG a universal matrix for doping with rare-earth and transition metal ions. The large yttrium ion is easily replaced by rare earth ions with different sizes from Ce^{3+} to Yb^{3+}.

The key factor determining the functional properties of YAG is the presence of defects. In YAG, such defects include oxygen vacancies, antisite defects (ADs), and various uncontrolled impurities. ADs (substitution defects) are formed in YAG crystals grown from the melt at high temperatures. In melt-grown YAG crystals, substitutions occur where Y^{3+} ions in dodecahedral c-nodes are replaced by Al^{3+} ions (Y_{Al})[12–19]. Schemes of these defects can be easily visualized using Fig. 1b. Theoretical calculations of the formation energy of various defects in YAG crystals show that ADs are predominant among all intrinsic defects of garnet host because their formation energy is significantly lower than that of Frenkel and Schottky defects[16–18]. ADs lead to the formation of electron and hole traps, significantly impacting the recombination processes in garnet-based scintillators. This

[1]Department of Technical Physics, L.N. Gumilyov Eurasian National University, Satbayev Str. 2, Astana 100000, Kazakhstan. [2]ISSP - Institute of Solid State Physics, University of Latvia, Kengaraga 8, Riga LV-1063, Latvia. [3]Department of Physics, Kazimierz Wielki University, Powstańców Wielkopolskich str., 2, Bydgoszcz 85-090, Poland. [4]Margulan University, Mira Str. 60, Pavlodar, Kazakhstan. ✉email: ak.dauletbekova@gmail.com

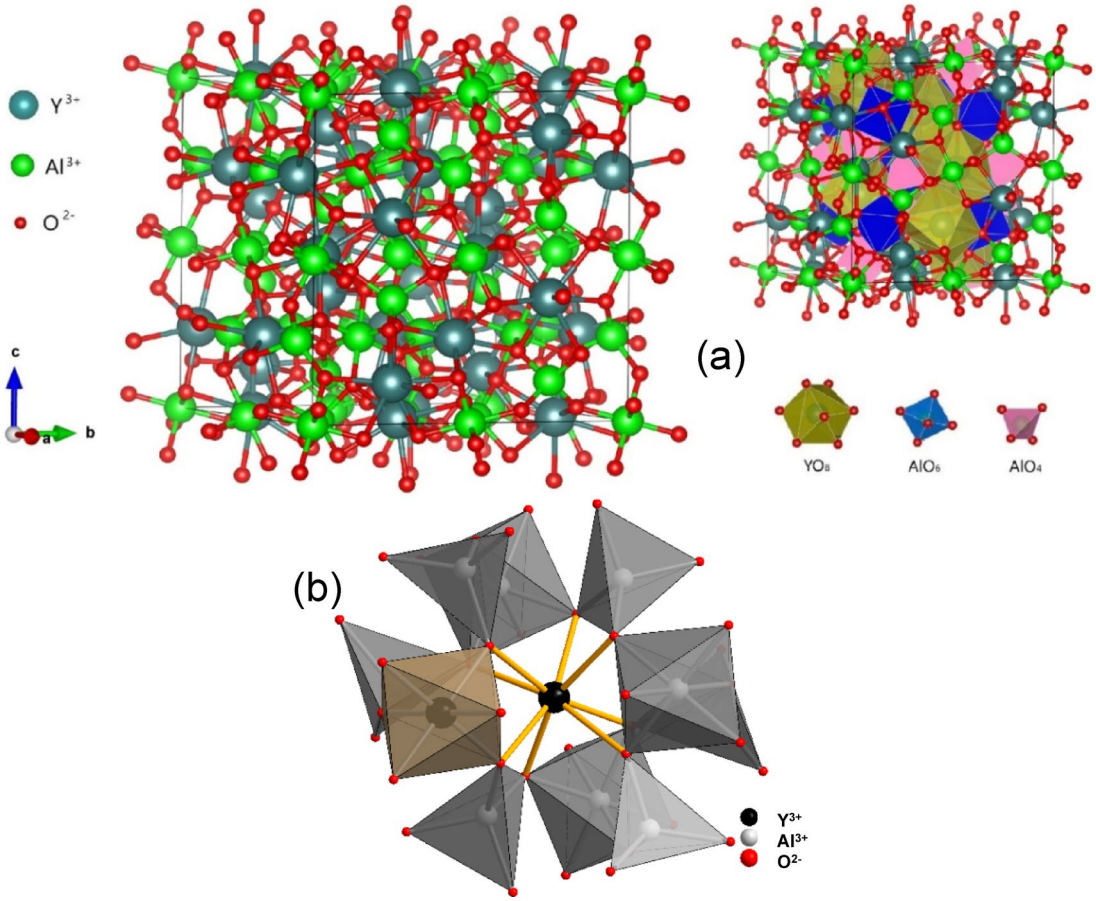

Fig. 1. (**a**) - Structure of $Y_3Al_5O_{12}$ garnet. The yttrium ion occupies the dodecahedral site while the aluminium ion occupies the octahedral and tetrahedral sites. (**b**) – the Y_{Al} antisite defect in the YAG host (Y^{3+} cations in the octahedral position of Al^{3+} cations).

particularly affects the kinetics of scintillation and contributes to a notable presence of slow components in the overall light output of scintillations[19,20].

YAG is one of the most essential advanced optical materials. YAG is a dielectric with a bandgap of approximately 8 eV, which corresponds to wavelengths shorter than 160 nm[1,3]. Due to the high bandgap of YAG, this garnet is an ideal host matrix for rare and transition metal ions such as Ce^{3+}, Pr^{3+}, Nd^{3+}, Er^{3+}, Yb^{3+}, Tm^{3+}, and Cr^{3+}. Within this energy gap are located energy levels associated with various defects and impurities in the garnet crystal structure. Consequently, doped YAG crystals are commonly used as solid-state lasers, illumination devices, phosphor converters in white LEDs, and scintillation techniques[4–8]. One critical aspect of their performance in harsh environments, such as nuclear reactors or space, is the radiation stability of the YAG host.

Melt-grown undoped YAG crystals with a large concentration of Y_{Al} ADs, as special analogues of cation isoelectronic impurities, were considered as prospective scintillation materials with emission in the UV range[9]. Furthermore, YAG crystals with a high concentration of one- and two-charged oxygen-vacancy defects (F^+ and F centers)also considered as thermoluminescent (TL) materias for the detection of different types of ionizing radiation[10]. In the context of these applications, the development of methods for precise tuning of the structure type, and concentration of various defect centers is an important task in the research of such advanced optical compounds, aimed at the supply of different crystalline forms of this material for specific practical needs. The interaction of these centers with AD and the formation of complex defects have not been sufficiently studied.

Radiation defects that occur during swift heavy ion (SHI) irradiation are of particular interest due to their unique interaction with materials. These ions simulate radiation damage caused by fission fragments of nuclear fuel. Additionally, ion irradiation allows for the rapid accumulation of radiation damage in materials used in nuclear reactor cores. In this case, energy transfer is exclusively localized, leading to the formation of tracks, vacancies, and nanostructures, as well as changes in the optical and structural properties of the crystal[21–37]. These effects simultaneously pose a threat of material degradation and open up new opportunities for its targeted modification. The studies of radiation defects in SHI-irradiated YAG are critical for its applications in high-energy optics detection, lasers, and scintillation detectors that operate under harsh radiation environments.

Optical spectroscopy is a powerful tool for analyzing such processes. Using different types of optical spectroscopy (e.g., absorption, luminescence and Raman spectroscopy, and their combination) we can reach to

observe: new absorption bands in the UV-visible range, associated with color centers (F^+ and F); new emission band connected with AD and F^+ and F emission centers; shifts and broadening of emission/excitation peaks, indicating amorphization or local disorder. Spectroscopic signatures provide insights into defect types, and concentrations, radiation tolerance thresholds. This approach also provides valuable insight into defect dynamics, and damage thresholds, supporting the development of radiation-resistant optical materials. Transmission electron microscopy, performed in transverse and longitudinal geometries, provides valuable information on the track parameters and its core structure which contributes to the development of radiation-resistant optical materials. The influence of tracks on AD formation has not been sufficiently studied.

Understanding the multifaceted nature of radiation effects occurring at the YAG garnet irradiated by SHI and investigating them with modern optical and structural methods, we will consider modifying material properties as a unified picture for considering possible applications.

Experimental methods

This work investigated the effects of $^{132}Xe^{22+}$ ions irradiation of pure YAG crystals from ALINEASON (Germany) with orientation (100), grown by the Czochralski method. The dimensions of the polished samples were 10 × 10 × 0.5 mm.

$Y_3Al_5O_{12}$ crystal samples were irradiated at the DC-60 cyclotron (Astana, Kazakhstan) with 230 MeV $^{132}Xe^{22+}$ ions to fluences of 6×10^{10}–10^{13} ion/cm^2, at room temperature (RT). The parameters of 230 MeV Xe ions are presented in Fig. 2, according to the SRIM code[38].

The specific ionization losses (electronic) S_e =25.2 keV/nm, and the elastic energy losses (nuclear) S_n= 0.08 keV/nm. The S_e/S_n ratio is 315 i.e., the electronic energy losses dominate over the nuclear energy losses. Thus, the main mechanism of defect creation is related to electronic excitations, but collisions should not be neglected. At the end of the 230 MeV Xe ion range, Sn locally increases and can lead to significant cascades of lattice ion displacements, the appearance of dislocation loops, defect aggregation, local amorphization, and Xe ion implantation (bubbles/pores). The concentration of Xe will be $\approx 4 \times 10^{16}$ atoms/cm^3 (fluence 10^{13}ion/cm^2) and 4×10^{15} atoms/cm^3 (fluence 10^{12}ion/cm^2). At the current stage of research, preference is given to the knock-on processes of defect creation.

The irradiated samples were investigated by optical absorption spectroscopy, which was accompanied by photoluminescence (PL) measurement under excitation by synchrotron radiation (SR). The optical absorption spectrum was measured using an Agilent Cary 7000 UMS universal spectrophotometer (Agilent, Santa Clara, USA). Investigations of the luminescence of YAG crystals were performed in the framework of II-2005-105 and II-20,090,087 projects at the Superlumi experimental station at DESY under excitation by synchrotron radiation with an energy of 3.7–25 eV at 7 K. Raman spectra were recorded using a TriVista 777 triple grating Spectrometer (TELEDYNE, USA).

Variation of hardness along the ion path was tested by an instrumented indentation unit G200 (Agilent, USA) in ambient air at RT using a Vicker's diamond tip. A nanoindentation technique with a constant indentation load of 4 g was used. The values of hardness (H) at nanoindentation tests were obtained using the Oliver–Pharr method[39]. Indentation tests were performed on samples prepared using the manual cleaving technique. The irradiated sample, together with an adjacent unirradiated piece, was placed on a smooth base with the irradiated surface facing down. Cleavage was performed from the upper unirradiated side using a sharp blade oriented perpendicular to the irradiated surface and along the crystal edge. At a fluence of 10^{11} Xe/cm^2, the obtained surfaces in the optical microscope look optically smooth and suitable for nanohardness measurements (hardness errors 3–5%). At a fluence of 10^{13} Xe/cm^2, a main part of the cleaved surfaces was also suitable for nanoindentation tests. However, at the end part of the ion range (> 11 μm) in the vicinity of the boundary between the irradiated and uniradiated zones, nanoindentation tests were omitted due to the bending of the cleaved surfaces under swelling - induced stresses. In the deeper unirradiated zone (distance about 20 μm) indentation tests show

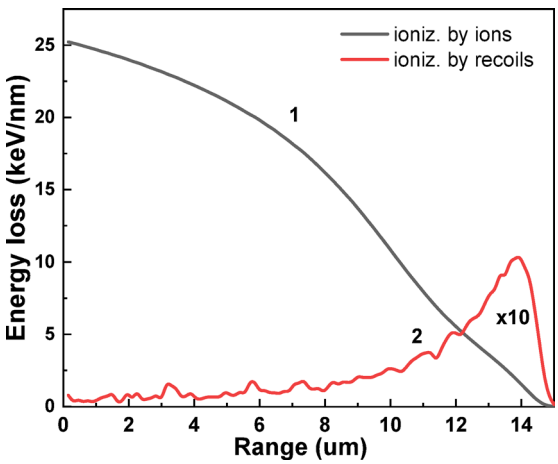

Fig. 2. Energy losses of 230 MeV $^{132}Xe^{22+}$ ions in YAG crystals: curve 1 - specific ionization losses S_e (electronic), curve 2 - elastic energy losses (nuclear) S_n.

hardness coinciding with that for the pristine crystal. The ion-induced change of hardness was calculated as $(H\text{-}H_0)/H_0$ (%), where H_0 denotes the hardness of a virgin crystal. The distance of indentation imprints from the irradiated surface serves as the depth parameter and was measured by means of optical microscopy.

Fei Tecnai G2 F20 Transmission electron microscope (TEM, Stanford, USA) was used for the imaging of tracks in YAG. Accelerating voltage was set to 200 kV, all the images were taken in the bright field mode. Thermo Fisher Scientific SEM Helios 5 UX for focused ion beam (FIB) lamellae preparation: Lamellae were prepared with Ga ion - powered FIB. 30 kV accelerated ions were used to prepare lamellae with a thickness below 100 nm. 5 kV accelerated Ga ions were used for the final polishing of the lamellae.

Results and discussion

High-resolution transmission electron microscopy

In Sect. 2, the parameters of the 230 MeV Xe ion in YAG were analyzed, where it is shown that the electronic energy losses S_e = 25.2 keV/nm and exceed the threshold energy of track formation in YAG, equal to 7.5 keV/nm[25].

To investigate single tracks, YAG samples irradiated at a fluence of 6×10^{10} ion/cm^2 were analysed using high-resolution TEM images (Fig. 3). At this fluence, the tracks have almost no overlap.

The unique sample preparation and study were conducted as follows: a large lamella (~12 µm wide) was cut from the side of the crystal using a focused ion beam and then polished. Then TEM was used to image the crystal perpendicularly to the ion tracks. Twenty sequential images were taken and combined forming one large, stitched image, which shows ion track propagation throughout the crystal. The red arrow corresponds to the ion beam direction. Underneath the stitched image, three selected images (Figs. 3b, c, and d) are shown. The colored frames are also shown in the upper image, therefore indicating which frame this is taken from.

The total length of the image in Fig. 3 is 20 µm. The length of the 230 MeV Xe YAG range according to SRIM is 15 µm. Figure 3 indicates that the tracks remain continuous until the midpoint of Fig. 3d. It shuld that the tracks are clearly visible. Comparison with the electron energy loss curve (Fig. 2) indicates that tracks are continuous in the loss region exceeding 10 keV/nm. When electronic energy losses are less than 10 keV/nm, chains of grains are formed and disappear at the end. At the end of the 230 MeV Xe ion penetration range, the nuclear stopping power (S_n) increases, which can trigger intensive cascades of lattice atom displacements, the formation of dislocation loops, defect clustering, local amorphization, and implantation of Xe ions in the form of bubbles or pores. Analyzing Fig. 3, we propose dividing the tracks morphology into three zones: a continuous track zone, a discontinuous track zone, and an end-of-track zone. All of this needs more research.

The images in Fig. 4 correspond to another lamella, which was taken from the crystal at 5 µm from the surface, however, now the lamella is taken perpendicularly to the ion tracks, therefore the ion tracks show up as white dots in the image.

The calculated ion track density, obtained from the image in Fig. 4b is ~ $(1.19 \pm 0.12) \times 10^{11}$ ion/cm^2, which matches well with experimental fluence. Image (Fig. 4c) shows higher resolution imaging of the ion tracks; two cases can be distinguished: in one, the crystal lattice is destroyed and amorphized (bright white). On the other hand, there are cases where the ion has slightly deformed the lattice (slightly darker, round contrast in the image, where the lattice can still be distinguished). Image (Fig. 4d) shows an even higher magnification image of a typical ion track defect in the lattice. Lattice deformation around the ion track can be seen, and the amorphized center of the track is well distinguished too.

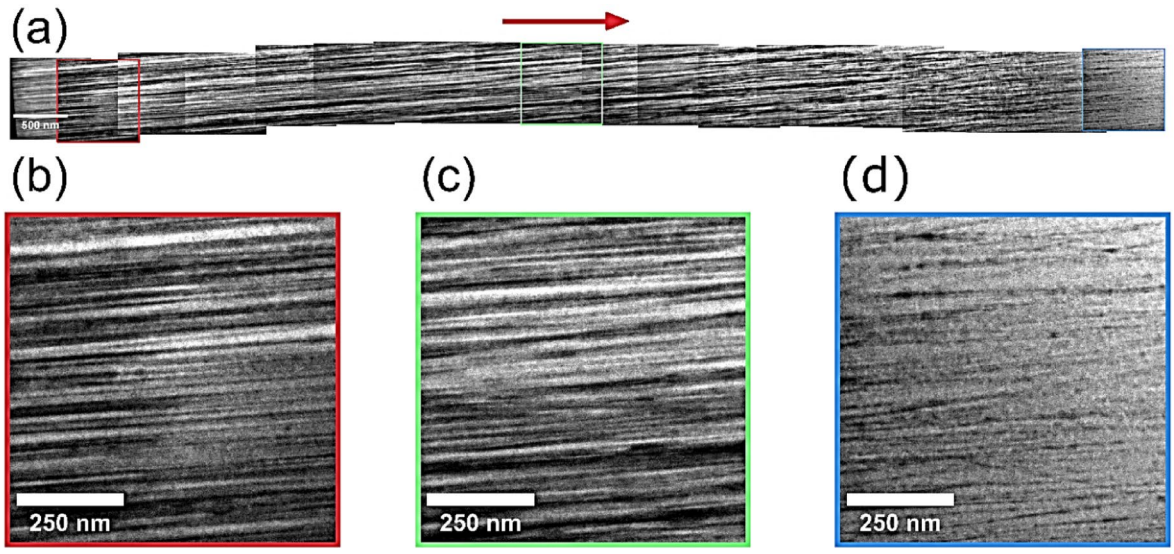

Fig. 3. 20-TEM sequential images along to the ion track. The direction of the ion beam (red arrow). YAG (100) single crystal was irradiated at RT with 230 MeV Xe ions up to fluences 6×10^{10} ion/cm^2.

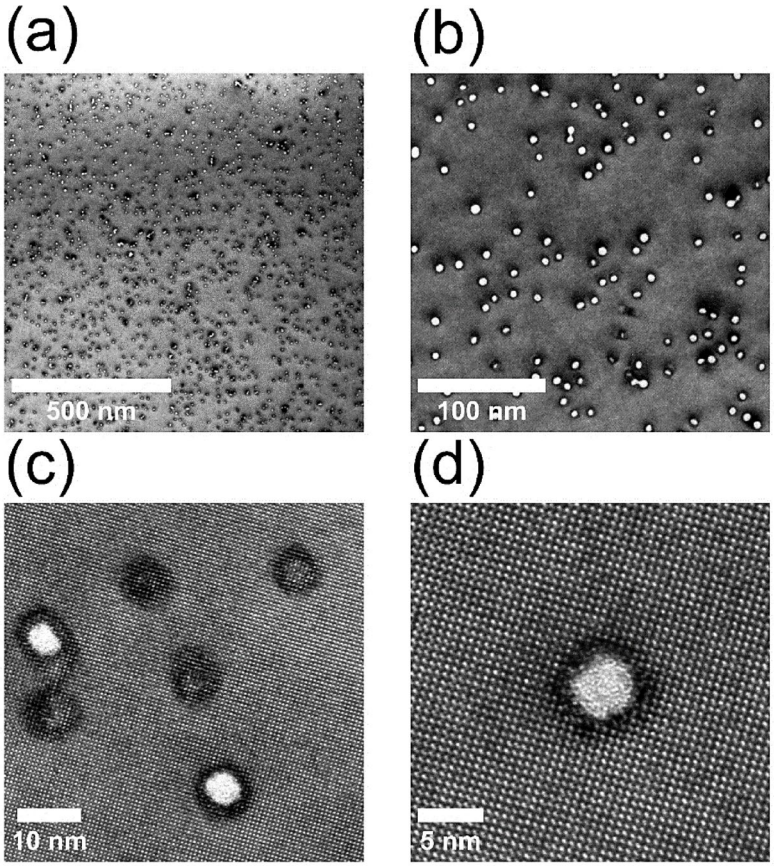

Fig. 4. HRTEM cross-section of YAG crystals irradiated at RT with 230 MeV Xe ions up to fluences 6×10^{10} ion/cm^2 variously magnified.

The transverse size of the central part (core) of the track is $d_c \approx (5.00 \pm 0.15)$ nm (estimation error ~1 pixel), as is the size of the deformed region around the core $d_d \approx (10.00 \pm 0.15)$ nm. It is evidenced that strong YAG amorphization starts at fluences of 10^{12} ion/cm^2 when track overlaps begin. Along with tracks, various point defects (color centers) are created, which are discussed in the next section.

As fluence increases, the distance between tracks decreases. When the average distance becomes comparable to the track diameter, overlap begins. Based on the track parameters, the track overlap threshold was assessed. The overlap threshold is not a strictly defined value. Fluence is often used when 50% of the surface area is covered, or when the average distance between centers is approximately equal to the diameter of the track. These estimates give similar values. The track overlap threshold can be calculated using a standard model. If ions strike randomly, then the projection of each track created onto a plane represents a circle with an area of $A = \pi \bullet (\frac{d}{2})^2$. The probability that a given point is covered by at least one track at a fluence φ (ion/cm^2) is equal to, according to the Poisson distribution: $P = e^{-\phi A}$, where A (nm^2) and φ (nm^{-2}). Then the formula for fluence with a given coverage f is: $= -\frac{\ln(1-f)}{A}$ For the deformed region around the track core, $d_d \approx (10.00 \pm 0.15)$ nm, A- 78.53982 nm^2. Then the fluence for 50% coverage is 8.8×10^{11} ion/cm^2, Thus, track overlaps begin at a fluence of 1×10^{12} ion/cm^2. Track overlaps lead to an increase in the degree of amorphization or defectiveness of the material, as well as changes in its mechanical and optical properties.

Both amorphous and crystalline cores have been found in the tracks. In addition, intermediate variants of a mosaic structure combining amorphous and crystalline areas have been observed. In addition, intermediate variants of a mosaic structure combining amorphous and crystalline areas are observed. It should note that the number of amorphous tracks dominates, which is consistent with the conclusions of the work[22,26,27]. The ratio between amorphous and crystalline cores is 70.3% and 9.4%, and 20.3% with a mosaic structure. Small variations in local energy density and thermal response of the lattice lead to a "mosaic" of tracks with different internal structures.

It is widely accepted that ion tracks are formed due to the local melting of the lattice along oft he ion path. The resulting nanohillocks are created by the ejection or swelling of molten material with lower density from the crystal surface. These features can be observed using the atomic force microscopy (AFM) method[22,29].

Figure 5 shows two-dimensional and three-dimensional topographies of YAG crystal surfaces after irradiation at RT with 230 MeV Xe ions up to fluences of 6×10^{10} ion/cm^2. During AFM measurements, the shape of defects is distorted because the cantilever is triangular with a finite tip radius. This occurs due to the triangular shape of the cantilever: its wide side edges do not allow it to accurately bypass the side walls of the defect, and the

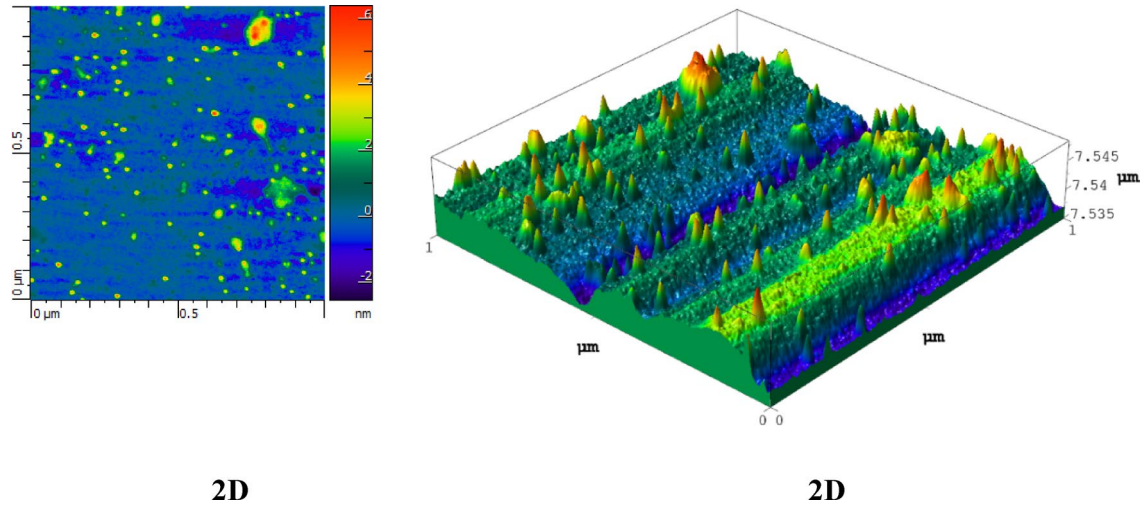

Fig. 5. 2D and 3D AFM images of YAG crystals irradiated at RT with 230 MeV Xe ions up to fluences 6×10^{10} ion/cm^2.

Center	Model	E_{abs}, [nm]	E_{abs},, [eV]	E_{em}, [eV]	E_{ex},, [eV]	Reference
F^+	v_O^{2+} + e	235 and 370	5.28 and 3.35	3.095 and 2.67 (at 10 K)	3.33; 5.37; 6.56; 7.3	20,30,41–43
F	v_O^{2+} + 2e	195 and 240	6.36 and 5.17	2.67 (at 10 K)	4.17 (weak); 4.9; ~6.6; 6.95	20,30,41–43
F^-	v_O^{2+} + 3e	360, 480 and 830	3.44, 2.58, 1.49			44
F^+ (Y_{Al}^{3+})	Perturbed F^+near Y_{Al}^{3+} AD	370, 235, and 200	3.35, 5.28, and 6.2	3.1		40
F^+(Fe^{2+})	F^+near impurity of Fe^{2+}	310	4.0			45
F_2	2(v_O^{2+} +2e)	239, 221	5.19, 5.61			41
O^-		400	3.1			46
F^+	v_O^{2+} + e			3.1	4.9; 5.37; 6.57, 6.93, 7.30	42
F	v_O^{2+} + 2e			2.69	4.165, 4.9; 6.57, 6.93	42

Table 1. Optical characteristics of defect centers in YAG crystals.

measured profile appears to be "stretched" to the sides. As a result, the probe cannot accurately follow the surface contours, especially in areas with overhanging or sharp features. As a result, the measured hillock appears more conical, and only their height can be reliably determined.

Analysis of the distribution of hillocks by height (Fig. 5) gives an average height of approximately h = 1.5 nm. The presence of nanohillocks on the surface leads to light scattering and reabsorption.

Optical absorption spectroscopy of YAG crystals

Various point defects are present in unirradiated YAG crystals grown from melt. The most well-known of these defects are Y_{Al}^{3+} AD and oxygen vacancies v_O^{2+}. According to[16–18]. The Y_{Al}^{3+} AD s special kinds of cation isoelectronic impurities are the most common defect in the YAG lattice because it has the lowest formation energy among all possible defects in the garnet structure. In the unirradiated YAG crystal, the concentration of Y_{Al}^{3+} ADs can even reach 0.1–0.2 at%. Oxygen vacancies v_O^{2+} are very effective traps for electrons. It can thus be filled by one or two electrons forming the one-charged F^+ and neutral F centers (electronic color centers), respectively (see Table 1). YAG crystals prior to irradiation may also contain F^+ (Y_{Al}^{3+}) complex defects[40] representing the F^+ center in the vicinity of Y_{Al}^{3+} ADs (Fig. 1) as well as F^- pair centers, e.g., two oxygen vacancies trapping 3 electrons.

Figure 6a The absorption spectra of irradiated YAG crystal samples irradiated at RT with 230 MeV ^{132}Xe ions up to fluences 6×10^{10} (curve1), 10^{11} (curve 2), 10^{12} (curve 3), and 10^{13} ions/cm^2 (curve 4). The absorption of the reference crystal was accounted for in the spectra. (b) - increase of absorption coefficient of the irradiated YAG crystals with respect to corresponding fluences: ($6 \times 10^{10} \rightarrow 10^{11}$) Xe/cm^2 (curve 1), ($10^{11} \rightarrow 10^{12}$) Xe/cm^2 (curve 2), ($10^{12} \rightarrow 10^{13}$) Xe/cm^2 (curve 3). Deconvolution of difference spectra: (c) ($6 \times 10^{10} \rightarrow 10^{11}$), (d) ($10^{11} \rightarrow 10^{12}$), (e) ($10^{12} \rightarrow 10^{13}$).

The analysis of the absorption spectra presented in Fig. 6a indicates the formation of color centers in YAG crystals that have been irradiated with 230 MeV Xe ions. (Table 1) demonstrates that the absorption bands of

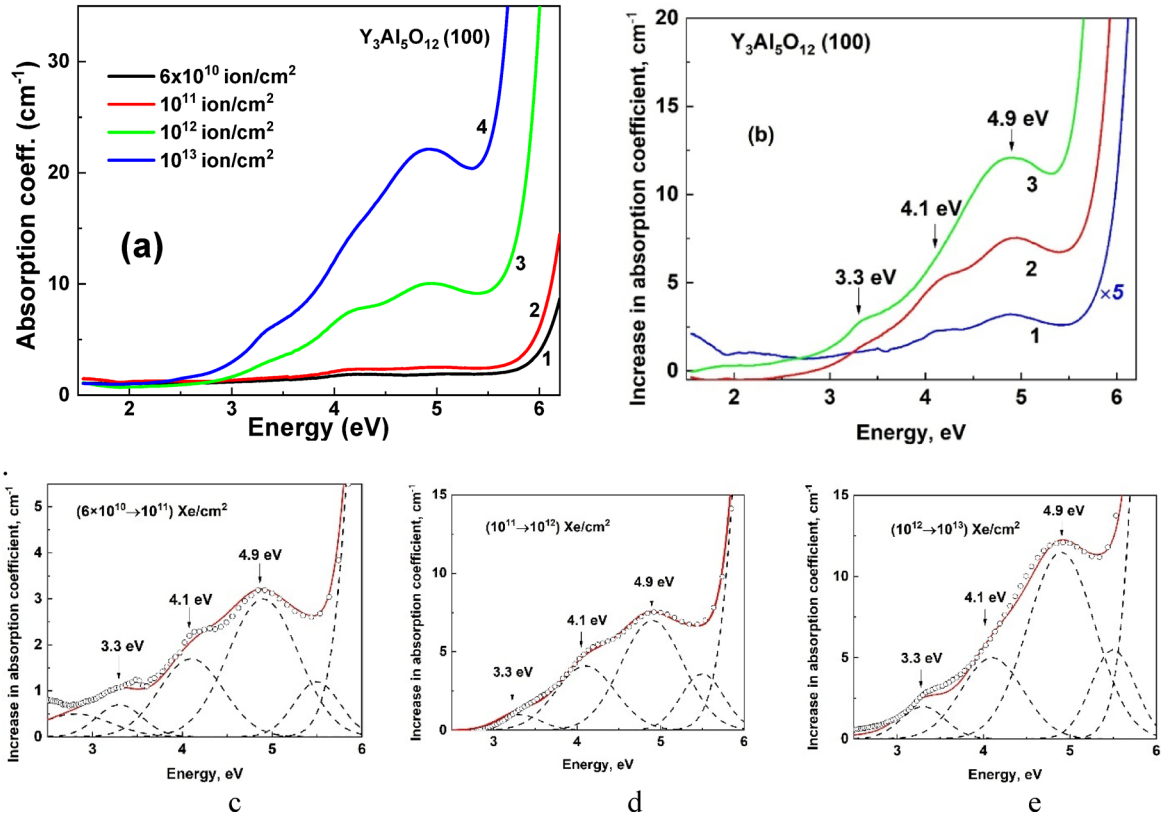

Fig. 6. shows the optical absorption spectra of YAG crystals irradiated with 230 MeV Xe ions as a function of fluence in the 6×10^{10}–10^{13} ion/cm^2 range.

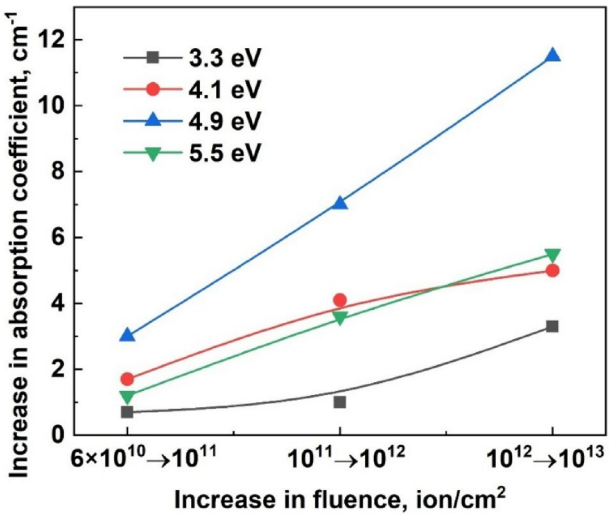

Fig. 7. Dependence of the increase in absorption at the absorption band maxima on the rise in fluence of YAG crystal samples irradiated at RT with 230 MeV Xe ions up to fluences 6×10^{10} – 10^{13} ion/cm^2.

the known centers overlap, complicating their analysis significantly. Despite this challenge, it can conclude, that as the irradiation dose increases, the quantity of point defect centers of various types in the irradiated samples also increases notably. Due to the overlap of absorption bands of defects, we used the method of difference of absorption spectra, which are shown in Fig. 6b. Deconvolution of difference spectra revealed several features (Fig. 6, c, d, e.). Figure 7 was constructed for analysis, showing the dependence of the increase in absorption at the absorption band maxima on the increase in fluence. f YAG crystal samples irradiated at RT with 230 MeV Xe ions up to fluences 6×10^{10} – 10^{13} ions/cm^2.

Figure 7 was created to analyze the relationship between the increase in absorption at the absorption band, maxima and the increase in fluence. This analysis is based on Figs. 6 (c, d, and e). Figure 7 demonstrates different behaviors of absorption increase at maxima of 3.3 eV, 4.1 eV, 4.9, and 5.5 eV with increasing fluence. It should be noted that absorption for all bands increases with increasing dose, but in different ways. The 4.9 eV band is increasing most intensively. The 4.1 eV band saturates with increasing fluence, consistent with its impurity nature— F^+(Fe^{2+}) center (Table 1).

The 5.5 eV band aligns with the 4.1 eV band and increases after a fluence of approximately 10^{12} ion/cm^2. The 3.3 eV band is characterized by a nonlinear increase, in contrast to the 4.9 eV and 5.5 eV bands, whose increase is practically linear. In addition, a sharp increase in the 4.9 eV, 5.5 eV, and 3.3 eV bands is observed with the onset of track overlap. This process is accompanied by the melting and cooling of track regions, creating conditions for the formation of AD. Therefore, the formation of centers such as "oxygen vacancies-AD" and "oxygen vacancy dimers-AD" should be considered. The 5.5 eV band is most likely associated with the F_2 dimer center, and F^+ center. The 3.3 eV band may be one of the bands of the F^+ (Y_{Al}^{3+}) center. The 4.9 eV band can be attributed to the perturbed F (Y_{Al}^{3+}) center. When such defects are created, one of the factors is most likely the recrystallization processes during track formation in YAG. According to simulations performed using MD (Molecular Dynamics) in the work[27], it is proposed to create amorphous tracks in YAG crystals irradiated with 167 MeV Xe ions. The creation of point defects, in this case, is associated with an increase in nuclear stopping power at the end of the ion path and with the implementation of the knock-on processes of defect creation. The work[22] assumes that the kinetics of structural transformations can be divided into (a) the formation of an initial molten state around the ion trajectory, and (b) the final phase transformation into a damaged structure during the relaxation process. At high levels of electron stopping power, a series of continuous tracks can be observed. Track parameters were predicted using iTS. It has been experimentally confirmed that YAG with a lower cation radius ratio $r_A/r_B = 1.68$ demonstrates a higher recrystallization effect within ion tracks. At ion energies ranging from 0.26 to 5.00 MeV/u and Se of 10.8 to 28.7 keV/nm for the YAG crystal, the observed damage morphology can be categorized into three distinct regions: (i) the undamaged region (below 1.48 eV per atom), (ii) the region of discontinuous tracks (between 1.48 and 2.02 eV per atom), and (iii) the region of continuous tracks (above 2.02 eV per atom). We have established that most of the tracks in a YAG crystal irradiated with 230 MeV Xe have an amorphous core, while some have a crystalline structure and a mosaic structure. It is precisely in the latter states of the track core, which are formed as a result of recrystallization processes. In addition, the deformed crystal shell around the track core, which is also formed during track creation, should be taken into account. This creates the conditions for the formation of ADs. We propose that track morphology can be divided into three zones: a continuous track zone, a discontinuous track zone, and the end-of-track zone. The structure of the track core of a continuous track may vary depending on the decrease in Se along the ion trajectory, ranging from amorphous to mosaic, and crystalline. The high local level of electronic losses is associated with the complex crystal structure of YAG, which leads to high local heating. Some electronic excitations can also create self-trapped exciton (STE), and localized exciton near AD LE(Y_{Al}), followed by the formation of defects associated with AD and oxygen vacancies. Another factor contributing to the creation of oxygen vacancies is the increase in displacements associated with increased nuclear stopping power at the end of the ion path and the implementation of the knock-on processes of defect creation.

Significant information can be obtained by examining the luminescent properties of irradiated samples. Due to the overlapping bands of the corresponding color centers, their further studies are related to the luminescence of these defects.

Luminescence spectroscopy of YAG crystals under SR excitation

The PL spectra of YAG crystals, irradiated by the Xe ions with fluences of 6×0^{10} and 10^{11} ions/cm^2 are presented in the Fig. 8a (curve 2 and curve 3) in comparison with the spectra of non-irradiated crystal as reference sample (curve 1) under excitation by SR with energy of 8 eV corresponding to the band gap value of YAG matrix[1–3]. The dominant emission band which peaked at 250 nm, is related to the luminescence of self-trapped excitons (STE) in YAG host[3,47]. The other two emission bands, peaked at 295 and 336 nm, are observed on the low energy side of this dominant STE emission band. These emission bands may be attributed to the luminescence of centers formed by the Y_{Al}^{3+} ADs in YAG host. Taking into account the interpretation of the nature of intrinsic luminescence of YAG crystal[3,47], emission in the 295 nm band can be caused by radiative relaxation of localized excitons near the Y_{Al}^{3+} AD (LE (Y_{Al}) centers) when the hole component of such an exciton localizes on the 2p levels of oxygen ions located in the vicinity of the AD and recombines with a free hole from the valence band. In the frame of this interpretation[3,43], the luminescence in the 336 nm band is caused by radiative relaxation of bound-state excitons, when the electron component of such an exciton localizes directly on the Y_{Al}^{3+} AD and recombines with a free electron from the conduction zone (BSE (Y_{Al}) centers).

The PL spectra of irradiated with fluence 6×10^{10} and 10^{12} ions/cm^2 and reference YAG crystals under excitation by SR with energies ranging from 5 to 7 eV are presented in Fig. 9.

This energy range of SR covers partly the transparency region and vicinity of YAG fundamental absorption[1,2,54] and is suitable for the excitation of the luminescence of F^+ and F centers in this material[47]. Namely, the luminescence of F^+ and F centers is observed even in the spectra of reference YAG crystal under SR excitation with an energy of 5.5 eV in the strongly overlapping bands with maxima at 400 and 460 nm[47], respectively (Figs. 9a; Table 1). The emission intensity of these centers, which is proportional to their concentrations, is relatively small, since the narrow emission bands of the background impurity of Tb^{3+} ions, associated with radiative transitions from the levels $^5D_3$ (a group of lines in the blue region of the spectrum at 384–450 nm) and levels $^5D_4$ (a group of lines in the green region of the spectrum at 480–575 nm), are well observed on the background emission bands of F^+ and F centers (Fig. 9a).

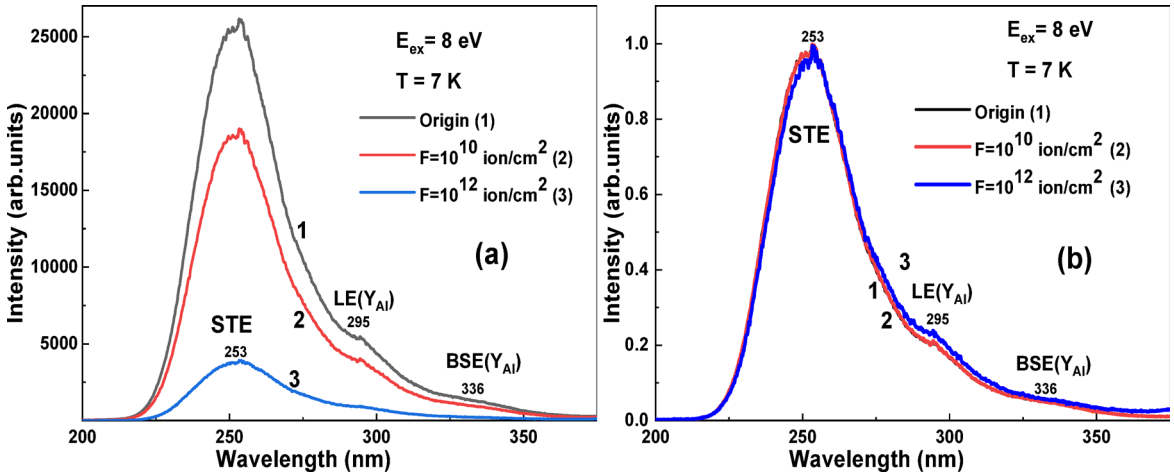

Fig. 8. PL spectra of YAG crystals irradiated with 230 MeV Xe ions to fluence 10^{10} and 6×10^{12} ion/cm^2 in comparison with spectra of initial YAG crystal under SR excitation with energy of 8 eV: (a) initial; (b) normalized.

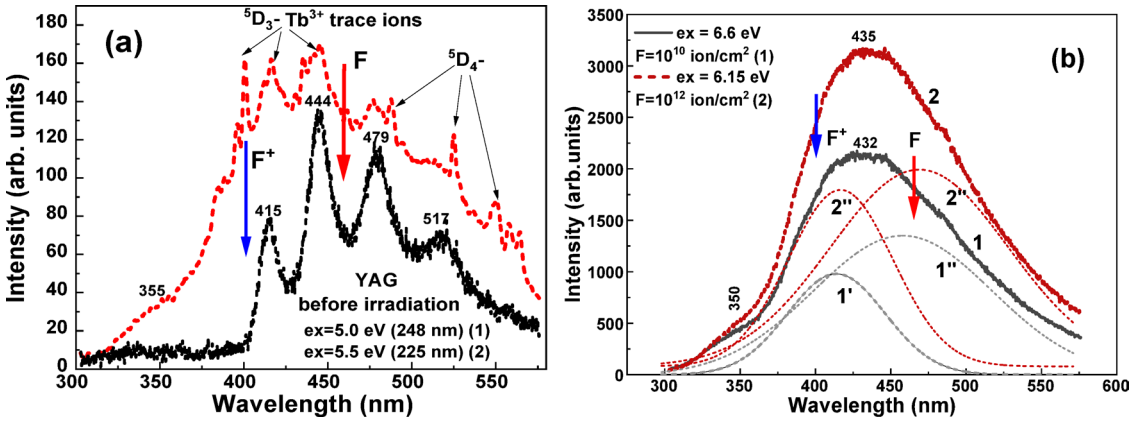

Fig. 9. (**a**) PL spectra of reference YAG crystal under excitation by SR at 5.0 eV (248 nm) (1) and 5.5 eV (225 nm) (2); (**b**) - luminescence of Xe-irradiated YAG crystals under SR excitation at 6.6 eV (188 nm) (curve 1) and 6.15 eV (201 nm) (curve 2) as a function of fluence of 6×10^{10} and 10^{12} ion/cm^2,T = 7 K. Curves 1′, 1″ and 2′, 2″ present the deconvolutions of curves 1 and 2 in Fig. 7b.

In the YAG crystal samples, irradiated by Xe ions with a fluence of 6×10^{10} ion/cm^2 and 10^{12} ion/cm^2, the concentration of F^+ and F centers significantly increases. This statement is evidenced the results of PL spectra measurements of these crystals under SR excitation with an energy of 6.6 eV and 6.15 eV, which shows an intense complex emission band peaking at 432 nm (Fig. 9b). Most probably, these dominant PL bands are caused by overlapping the F centers emission band with a maximum at 460 nm and emission band of F^+ centers peak at 400 nm (Fig. 9b). It should be noted that the ratio of luminescence intensity of F^+ and F centers in the corresponding bands at 400/460 nm, equal to 0.9 for the reference crystal (Fig. 9a), remains the same for the irradiated samples (Figs. 9b, curved 1 and 2).

In more detail, the change of the shape of PL spectra in the range of F-like center emission bands with the increase of Xe ions irradiation fluence are presented in Fig. 10. With fluence rising, the intensity of PL bands peaked at 400 nm and 460 nm, related to the F^+ and F centers, began to dominate. As can be seen from Fig. 10, the number of these defects is much higher than that in the unirradiated crystal. This indicates the formation of a large quantity of oxygen vacancies in the YAG crystal during irradiation by 230 MeV Xe ions.

The possibility of forming absorption and luminescence of pair centers, such as "oxygen vacancy-AD" and "oxygen vacancy dimers", should also be taken into account. Specifically, Fig. 10b indicates that the irradiated crystal exhibits additional luminescence bands peaking around.

347–350 nm as well as PL emission band at wavelengths above 550 nm, which may be associated with these centers. We mentioned the existence of such centers in the Section devoted to the absorption spectra.

PL excitation (PLE) spectra of STE and LE(Y_{Al}) centers luminescence in the 6–12 eV range YAG crystal samples irradiated by Xe ions to fluence 6×10^{10} ion/cm^2 (curve 1) and 10^{12} ion/cm^2 (curve 2) in comparison with spectra of reference YAG crystal (curve 1) are presented in Fig. 11.

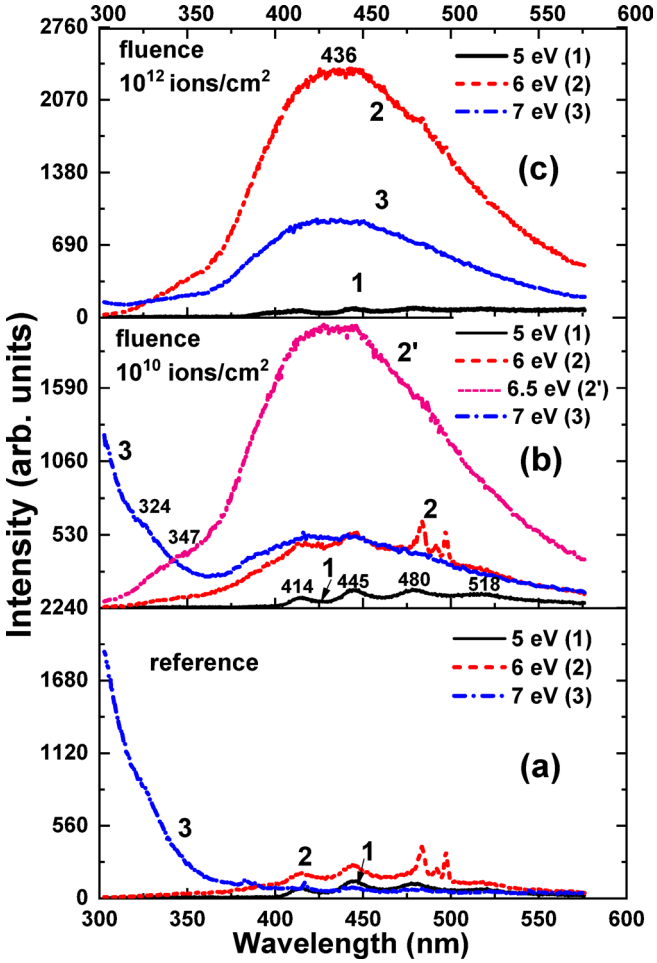

Fig. 10. PL spectra in the YAG crystals: (**a**) reference crystal; (**b**, **c**) - irradiated with 230 MeV Xe ions to fluence 6×10^{10} ion/cm^2 and c)10^{12} ion/cm^2, under SR excitation with selected energies of 5 eV (1), 6 eV (curve 2), 6.5 eV (curve 2") and 7 eV (curve 3). Curves 2′′ and 2"′ present the deconvolutions of curve 2′ in Fig. 8b, while curves 2 and 2″ represent the deconvolutions of curve 2 in Fig. 8c.

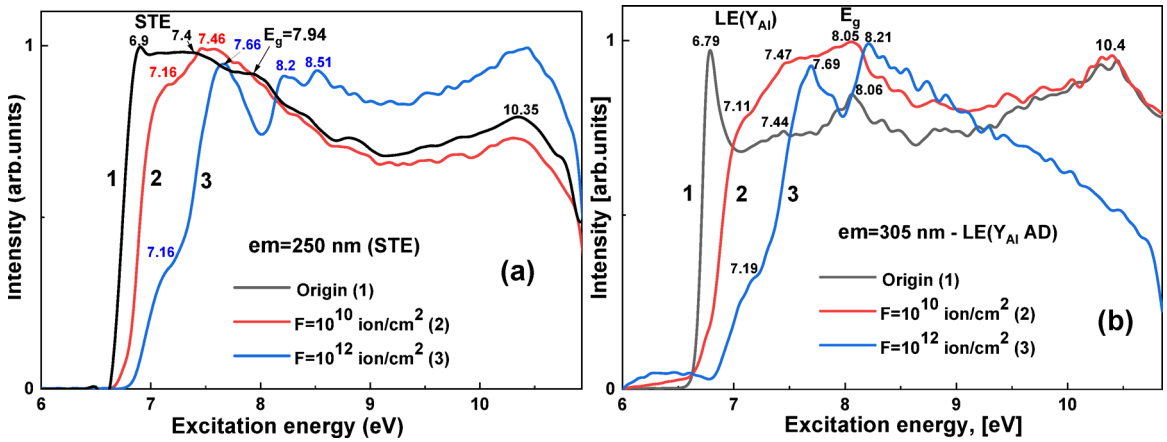

Fig. 11. (**a**) PLE spectra of YAG crystal samples irradiated with 230 MeV Xe ions to fluence 6×10^{10} ion/cm^2 (curves 2) and 10^{12} ion/cm^2 (curves 3) in comparison with reference YAG crystal (curves 1) under SR excitation in the energy range of 5.5–7.5 eV, registered in STE band peaked at 250 nm, and (**b**) LE (Y_{Al} AD) band peaked at 300 nm. T = 7 K.

In accordance with[3], the STE luminescence in the band peaked at 250 nm in the reference YAG crystal is excited in the dominant bands peaked at 6.9 eV and 7.4 eV (Fig. 11a, curve 1) corresponding to the transitions from ground state to the singlet and triplet excited levels of STE, and in the band peaked 7.94 eV, corresponding to the energy bandgap E_g of YAG host at 9 K[3,47]. In irradiated samples, the intensity of STE emission significantly decreases (Fig. 8a), and the corresponding changes are observed in the PLE spectra of these samples registered at 250 nm. Namely, STE- related bands in PLE spectra of YAG crystal irradiated to a fluence of 6×10^{10} ion/cm^2 practically diminish, and other dominant PLE bands peaked at 7.16 and 7.46 eV are observed. Furthermore, in the YAG crystal irradiated with a large fluence of 10^{12} ions/cm^2, the intensity of 7.16 eV PLE band is strongly decreased and other PLE excitation bands peaked at the 7.66 eV, 8.2 eV, and 8.51 eV are observed. Most likely, these significant changes are associated with the onset of YAG lattice destruction and amorphization within the ion track.

The luminescence of LE (Y_{Al} AD) centers in the reference YAG crystal, registered at 305 nm in the vicinity of emission band of these centers peaked at 295 nm, is excited in the sharp band peaked at 6.79 eV and wide band peaked at 7.46 eV (Fig. 11a, curve 2), both related to the transitions from ground state to the singlet and triplet excited levels of these centers, as well as in the PLE band peaked at 8.06 eV, most probably corresponding to the energy bandgap E_g of YAG host[10,42]. In the YAG crystal sample, irradiated to fluence of 10^{10} ions/cm^2, the LE (Y_{Al} AD) related bands in PLE spectra are fully diminished, and other PLE bands peaked at 7.11 and 7.46 eV, as well as the band peaked at 8.05 eV are observed. In turn, in YAG crystal irradiated with a large fluence of 10^{12} ion/cm^2, when tracks overlap, the intensity of the 7.11 eV band strongly decreases, and other PLE excitation bands, peaked at 7.69 eV and 8.21 eV, are registered. These significant changes of PLE spectra of LE (Y_{Al} AD) centers can also be caused by the start of YAG lattice destruction and amorphization within the ion tracks.

The above-mentioned features of PLE spectra (Fig. 11) show that the irradiation of YAG crystals with 230 MeV Xe ions with fluence 6×10^{10} and 10^{12} ion/cm^2 lead to the destruction of conditions for the formation of STE and LE (Y_{Al} AD) emission centers under SR excitation and creates another more complex emission centers in them. Most likely that, the forming absorption and luminescence of pair centers, like "oxygen vacancy-ADs" and "dimers of oxygen vacancy-ADs" should be considered here. Namely, Fig. 10 also indicates that other luminescence bands peaked at wavelengths of 420, 445, 480, and 545 nm exhibit the irradiated crystal, which may be associated with "oxygen vacancy dimers" or "more complex oxygen vacancy related centers". We mentioned the existence of such centers in the Section, devoted to absorption spectra.

The PLE spectra of F centers emission band, registered at 440–445 nm in reference YAG crystal, as well as in YAG crystals, irradiated to fluence of 6×10^{10} ion/cm^2 and 10^{12} ions/cm^2, are presented at Fig. 12. The F centers emission in reference YAG crystals is exciting in the PLE band, peaking at 4.95, 6.02 and 6.6 eV. The first two PLE bands correspond to the intrinsic $^1S \rightarrow {}^3P$ and ^1P transitions of F centers, respectively, while the last band corresponds to the energy creation of excitons bound with F centers[35]. The low intensive bands, peaked at 5.66–5.6 eV range, can correspond to PLE bands of F^+ centers, which strongly overlap with the luminescence of F centers in YAG crystals. Generally, such results are in good correlation of the main results presented in work[42].

Xe ions irradiation with fluence of 6×10^{10} ion/cm^2 and 10^{12} ion/cm^2 leads to significant changes in the PLE spectra of YAG crystals (Fig. 12). Namely, the main exciton band of F center luminescence at 445 nm peaked around 6.6 eV become much higher and broader and slightly shifted in the low energy range to 6.57 eV in YAG crystal irradiated with fluence of 10^{10} ions/cm^2 (curve 2). Furthermore, the PLE spectrum, registered at 550 nm, shows an additional band peaked at 5.41 eV (curve 4). That indicates complicity of the emission bands peaked at 430 nm (Fig. 10b), and overlapping the different bands related to the various F- like centers. In turn, the main exciton band of F center emission, registered at 440 nm in YAG crystal irradiated with the largest fluence of 10^{12}

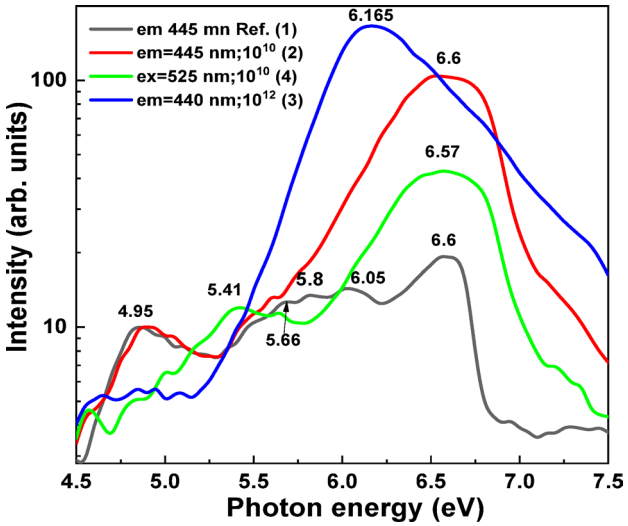

Fig. 12. PLE spectra of emission registered at 440–445 nm (1, 2, 4) and 525 nm (curve 4) in reference YAG crystal (curve 1) and YAG crystals irradiated to fluence of 6×10^{10} ion/cm^2 (curve 2) and 10^{12} ion/cm^2 (curve 3).

ions/cm^2, is very broad and significantly shifted to 6.165 eV (Fig. 12, curve 2). Interesting that the intensity of the PLE band in this sample decreases significantly. Therefore, the irradiation with fluence of 10^{12} ions/cm^2 leads to full destruction of the structure of defect-related luminescent centers, which are realized in as grown YAG crystals, and creation of a variety of more complex oxygen-vacancy defect related emission centers with different luminescent characteristics in the comparison with isolated F^+ and F centers in this garnet host.

Concluding, with increasing fluency of Xe irradiation, the PL and PLE bands of F^+ and F centers begin to dominate (Figs. 10 and 11). Thus, the concentrations of these defects in irradiated YAG crystals are much higher than in the unirradiated sample. This indicates the formation of large concentrations of oxygen vacancies during irradiation by 230 MeV Xe ions. The formation of AD-oxygen vacancy defects during 230 MeV irradiation with Xe ions can also be assumed. The process can be stimulated by the creation of tracks. As we know, the formation of tracks within the thermal spike model leads to the melting of the area surrounding the ion path, followed by cooling[22,27], 48–[51]. This creates conditions that promote the emergence of different kinds of defects and related with them emission centers during irradiation with 230 MeV Xe ions mainly due to the high energy losses (Table 1).

Finally, to better illustrate the transformation of high-energy excitation into low-energy emission in YAG crystals, the scheme of the excitation and emission processes of various intrinsic and defect-related centers, under excitation of the respective excitons by SR near the fundamental absorption edge of the YAG host, is presented in Fig. 13.

Raman and hardness analysis

It is known that YAG crystals are amorphized by SHI irradiation with the threshold S_e value of 7.5 keV/nm[25]. In our case, S_e = 25.2 keV/nm, which significantly exceeds the mentioned threshold value. The effect of amorphization can be clearly observed in Fig. 14, which illustrates the dependence of the Raman spectra of YAG single crystals on fluence.

Table 2 shows the experimental Raman active mode frequencies[48,49], as a function of fluence. The data are given from the analysis of Fig. 13.

The study[54] shows that the A_{1g} modes have a molecular character and can be classified as internal, and external modes of tetrahedral subunits of AlO_4. Three intense, pronounced A_{1g} modes can be seen for the unirradiated crystal, and irradiated up to a fluence 6×10^{10} ion/cm^2 and a broadening of the bands in the region of 1200–1500 cm^{-1} is observed for the irradiated sample.

According to the analysis[52,55], the low-frequency modes mainly correspond to the translational motion of heavy Y atoms, with minor contributions from rotational and translational motion, and to the ν_3 vibrational modes of AlO_4 tetrahedra. The medium-energy modes are due to the quadrupole (ν_2) molecular mode, and the high-energy modes contain mainly the respiratory (ν_1) and (ν_4) molecular modes of AlO_4[50]. Upon irradiation to a fluence of 1×10^{12} cm^{-2}, the bands 566, 715, 400, 545 ν_3 (AlO_4), 689 $\nu_1 + \nu_4$ (AlO_4), 715, 854 cm^{-1} disappear in the Raman spectrum. Increasing fluence to 1×10^{13} cm^{-2}, results in the vibrational modes (370, 162 Y, 401, и 260 Translation + Rotation + ν_3 (AlO_4) cm^{-1} remaining in the Raman spectrum, their intensity is significantly reduced. Thus, an increase in fluence leads to a progressive loss of translational symmetry. According to[37], this occurs when statistical disorder expands into translational modes. The progressive loss of translational symmetry due to static lattice disorder broadens these modes. Peaks 545 ν3 (AlO_4), 689 ν1 + ν4 (AlO_4), associated with tetrahedral blocks, begin to disappear from the beginning of track overlap. At the same time, a broad, low-intensity band with a maximum in the region of 545 cm^{-1} is observed. This indicates the emergence of amorphous regions. The 162 cm^{-1} band associated with Y decreases sharply starting at a fluence of 10^{12} ion/cm^2. Dodecahedral blocks begin to disappear, but some remain even at high fluences.

It should be noted that the high-energy modes have already begun to broaden at a fluence of 6×10^{10} ion/cm^2. These bands are more sensitive to the beginning of the amorphization of the material. Considering SHI's

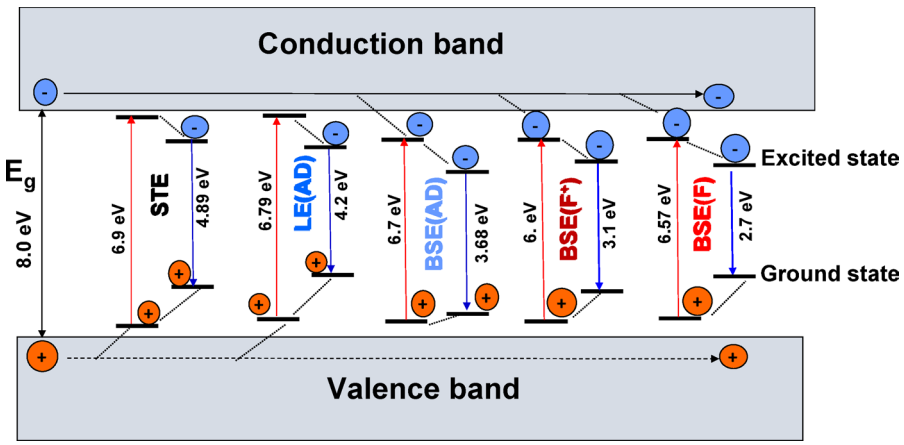

Fig. 13. Scheme of the excitation and emission processes of the STE, LE(AD), BSE(AD), BSE(F^+), and BSE(F) centers under excitation of the respective excitons by synchrotron radiation near the fundamental absorption edge of the YAG host.

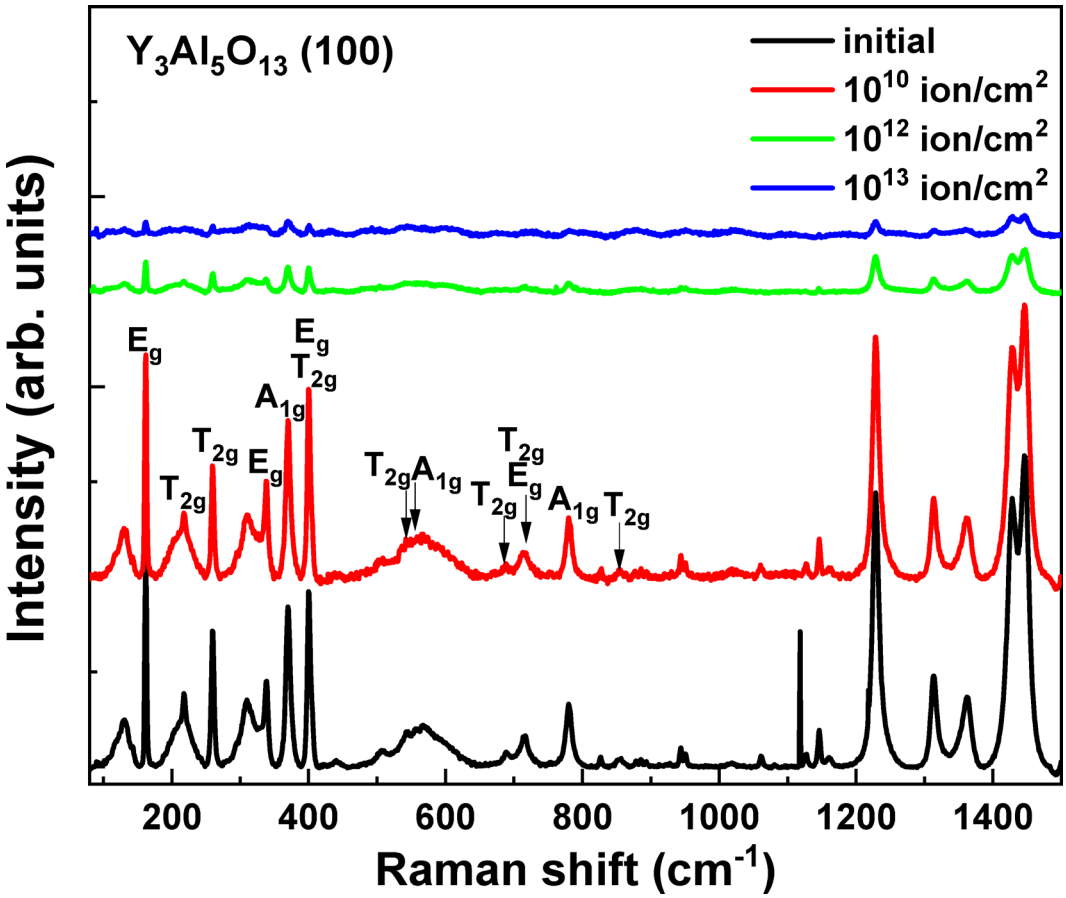

Fig. 14. Raman spectra of YAG (100) single crystal irradiated at RT with 230-MeV ^{132}Xe ions up to fluences 6×10^{10} –10^{13} ion/cm^2.

high level of influence, it can be stated that, starting at a fluence of 10^{12} ion/cm^2, chemical bonds are destroyed due to track overlapping, melting, and cooling. The appearance of amorphous regions was also detected in YAG: Ce crystals by XRD. XRD analysis showed changes in the degree of crystallinity of YAG: Ce crystals irradiated with 230 MeV Xe ions, depending on the fluence[56] The initial sample showed 100% crystallinity. Irradiation at a fluence of 10^{12}ion/cm^2 reduced the crystallinity to 98.32%. A fluence of 10^{13} ion/cm^2 further reduced crystallinity to 83.32%, and to 70.47% for a fluence of 10^{14} ion/cm^2. Beginning with a fluence of 10^{12} ion/cm^2, the authors observed the formation of an amorphous halo in the X-ray diffraction patterns, specifically in the 2θ range of 23.5° to 46.5°. This observation indicates that radiation damage and the breaking of chemical bonds have led to the disruption of the crystal structure. An amorphous contribution has been evident since 10^{11} ion/cm^2, and a decrease in material density has been observed.

The 230 MeV Xe ion irradiation process causes partial amorphization of the YAG in the near-surface layer structure. This results in a decrease in density, an increase in microdeformation, and a rise in dislocation density. Together, these changes indicate the destruction and destabilization of the original crystalline phase. Indeed, nanoindentation measurements on YAG samples irradiated at fluence 10^{13} ion/cm^2 show a significant softening (60% hardness reduction), indicating amorphization (Fig. 15)).

.

Softened zone expands to a distance about 11 μm, where the threshold electronic energy loss from the data of Fig. 2 decreases to ~7 keV/nm. Irradiation at 10^{11} ion/cm^2 did not result in softening and maintained pristine hardness. Clearly, the stage of track overlap needed for a change in hardness has not been achieved. Individual tracks do not significantly affect hardness.

Conclusion

Single crystal YAG samples were irradiated with 230 MeV Xe ions at the DC-60 accelerator at fluences ranging from 6×10^{10} to 1×10^{13} ion/cm^2. A characteristic feature of this type of irradiation is that the electronic ionization losses of S_e significantly exceed the nuclear energy losses of S_n, and the S_e/S_n ratio is equal to 315. The average range of 230 MeV Xe ions in YAG host is 14.5 μm. The irradiated crystals were characterized using optical absorption spectroscopy, photoluminescence (PL) spectroscopy under synchrotron radiation excitation, Raman spectroscopy, hardness testing, and high-resolution transmission electron microscopy (HRTEM).

Mode symmetry	Exp., ω_{exp}(cm^{-1})[52],	Exp. ω_{exp}(cm^{-1})[53],	Exp. ω_{exp} (cm^{-1}) Virgin	Fluence 6×10^{10} (cm^{-2})	Fluence 1×10^{12} (cm^{-2})	Fluence 1×10^{13} (cm^{-2})	Vibration [b)]
A_{1g}	370	373	370	370	370	370	
A_{1g}	559	556	567	566			
A_{1g}	783	784	780	780	780		
E_g	163	164	162	162	162	162	Y
E_g	310		310	310	310		
E_g	340	340	339	338	337		
E_g	402		400	400	400	401	
E_g	523						
E_g	536						
E_g	712	720	716.5	715			
E_g	754						
T_{2g}	45						
T_{2g}	220	220	218	218	218		Translation
T_{2g}	243						
T_{2g}	261	263	259	259	260	260	Translation + Rotation + ν_3 (AlO_4)
T_{2g}	295						
T_{2g}	361						
T_{2g}	372						
T_{2g}	406	403	400	400			
T_{2g}	438						
T_{2g}	545	544	545	545			ν_3 (AlO_4)
T_{2g}	691	690	689	689			$\nu_1+\nu_4$ (AlO_4)
T_{2g}	718	720	716	715			
T_{2g}	857	857	854	854			

Table 2. Characteristics of Raman spectra.

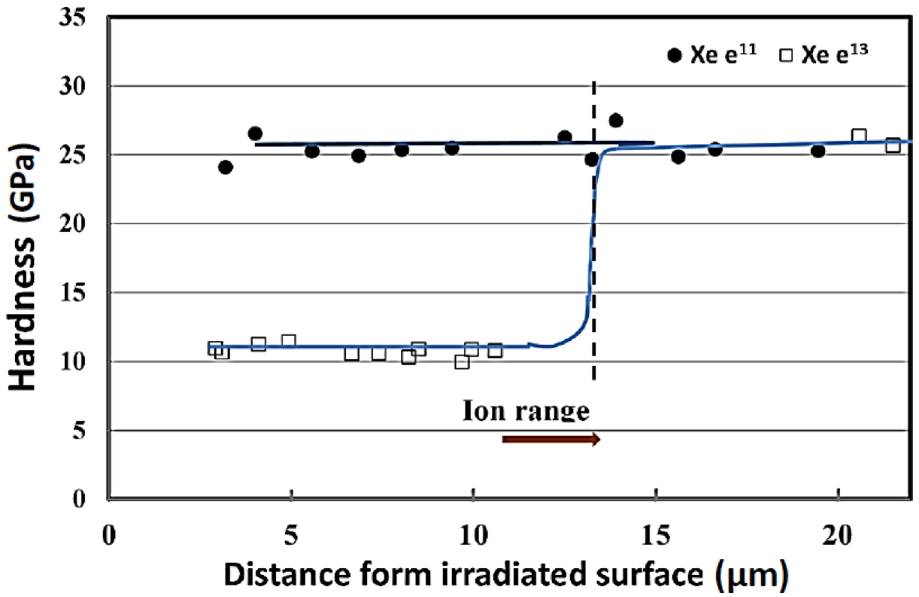

Fig. 15. The relationship between the hardness of YAG and the penetration depth of 230 MeV ions at fluencies of $Xe^{11}$and Xe^{13} cm^2.

The obtained results indicate that the concentration of point defects increases progressively with ion fluence. Optical absorption spectra revealed the formation of color centers, whose behavior depends on irradiation fluence. Difference absorption spectra with deconvolution reveal several features. It has been established that the maxima of the absorption bands at 4.1 eV, 4.9 eV, 5.5 eV, and 3.3 eV change differently with increasing ion irradiation fluence. The 4.1 eV band saturates at high doses, confirming its impurity nature and connection with the $F^+(Fe^{2+})$ center. The 4.9 eV and 5.5 eV bands increase approximately linearly with fluence, whereas the 3.3 eV

band exhibits nonlinear growth. When ion tracks begin to overlap, a pronounced increase in the 4.9 eV, 5.5 eV, and 3.3 eV bands is observed, likely due to localized melting and rapid cooling processes within the track regions. These conditions appear favorable for the formation of complex defects such as "oxygen vacancy–antisite defect (AD)" and "oxygen vacancy dimer–AD" centers. The 5.5 eV band can be associated with F_2 dimer and F^+ centers, while the 4.9 eV and 3.3 eV bands are likely linked to perturbed F (Y_{Al}^{3+}) and F^+ (Y_{Al}^{3+}) centers, respectively.

The presence of the Y_{Al}^{3+} antisite defects and one-charged and two-charged oxygen vacancies (F^+ and F centers, respectively) was also established using PL of reference and irradiated crystals under excitation by SR at 9 K. The PL band peaked at 250 nm corresponds to the emission of self-trapped excitons, while the PL bands peaked at 295 and 336 nm are caused by radiative relaxation of excitons localized at and bound with Y_{Al}^{3+} ADs. The concentration of F^+ and F emission centers in the overlapping bands peaked at 400 nm and 460 nm, respectively, and strongly increased with the fluence of irradiation. We presuppose also creation of dimers based on the F-like centers and Y_{Al} ADs. Such Y_{Al} AD — F^+ and or Y_{Al} AD — F pair centers can be created not only during crystal growth but also during heavy ion irradiation.

At higher fluences, Raman spectroscopy revealed progressive broadening of high-frequency modes beginning at 1×10^{10} ion/cm^2, suggesting its high sensitivity to early structural disorder. Beyond 1×10^{12} ion/cm^2, significant bond disruption and structural degradation occur, most likely due to track overlap and localized melting–quenching processes.

This suggests that mechanical changes, such as reduced hardness, are less sensitive indicators of track formation and amorphization effects than detailed spectroscopic measurements. HR TEM analysis confirmed the presence of continuous tracks at energy losses above 10 keV/nm, whereas lower-energy tracks appear as chains of smaller defects. The core track diameter measures approximately $d_c \approx (5.00 \pm 0.15)$ nm (estimation error ~ 1 pixel), with a surrounding damaged region $d \approx (10.00 \pm 0.15)$ nm, indicating significant amorphization at higher fluences. The ratio between amorphous and crystalline cores is 70.3%, 9.4% and 20.3% with a mosaic structure.

Data availability

All data generated or analysed during this study are included in this published article.

Received: 3 July 2025; Accepted: 28 October 2025
Published online: 27 November 2025

References

1. Zorenko, Y. Luminescence of excitons and antisite defects in the phosphors based on Garnet compounds. *Radiat. Meas.* **38**, 677–680. https://doi.org/10.1016/j.radmeas.2004.02.009 (2014).
2. Zorenko, Y., Konstankevych, L., Mikhailin, V., Kolobanov, V. & Spasskii, D. Luminescence of excitons in Single-Crystal garnets. *Opt. Spectrosc.* **96**, 390–397. https://doi.org/10.1134/1.1690031 (2004).
3. Zorenko, Y. Exciton and antisite defect–related luminescence in $Lu_3Al_5O_{12}$ and $Y_3Al_5O_{12}$ garnets. *Phys. Stat. Sol (b)*. **244**, 2180–2189. https://doi.org/10.1002/pssb.200642431 (2007).
4. Lupei, V. & Lupei, A. Nd:YAG at its 50th anniversary: still to learn. *J. Lumin.* **169**, 426–439. https://doi.org/10.1016/j.jlumin.2015.04.018 (2016).
5. Nandi, P., Goswami, M., Arya, A. & Krishnan, M. Study of crystallization kinetics, microstructure and optical properties of ce: YAG glass-ceramics for white LED applications. *J. Therm. Anal. Calorim.* **147**, 3007–3013. https://doi.org/10.1007/s10973-021-10690-w (2022).
6. Borlaf, L., Mario, Frankowska, M., Kubiak, W. W. & Graule, T. Strong photoluminescence emission at low Dopant amount in yag:ce and yag:eu phosphors. *Mater. Res. Bull.* **100**, 413–419. https://doi.org/10.1016/j.materresbull.2018.01.005 (2018).
7. Zapadlík, O., Nikl, M., Polák, J., Průša, P. & Linhart, V. Engineering of yag:ce to improve its scintillation properties. *Opt. Mater. X.* **15**, 100165. https://doi.org/10.1016/j.omx.2022.100165 (2022).
8. Pankratov, V. et al. Peculiarities of luminescent properties of cerium doped YAG transparent nanoceramics. *Radiat. Meas.* **45**, 392–394. https://doi.org/10.1016/j.radmeas.2009.12.014 (2010).
9. Zorenko, Y. Luminescence of isoelectronic impurities and anti-site defects in garnets. *Phys. Stat. Sol (c)*. **2**, 375–379. https://doi.org/10.1002/pssc.200460275 (2005).
10. Jia, L. Effect of carbon doping on F-Type defects in YAG and yag:ce crystals. *Phys. Stat. Sol (b)*. **258**, 2100325. https://doi.org/10.1002/pssb.202100325 (2012).
11. Euler, F. & Bruce, J. A. Oxygen coordinates of compounds with Garnet structure. *Acta Cryst.* **19**, 971–978. https://doi.org/10.1107/S0365110X65004747 (1965).
12. Ashurov, M. K., Voronko, Y. K., Osiko, V., Sobol, A. & Timosheckin, M. Spectroscopic study of stoichiometry deviation in crystals with Garnet structure. *Phys. Stat. Sol (a)*. **42**, 101–110. https://doi.org/10.1002/pssa.2210420108 (1997).
13. Dong, J. & Lu, K. Noncubic symmetry in Garnet structures studied using extended x-ray-absorption fine-structure spectra. *Phys. Rev. B*. **43**, 8808–8821. https://doi.org/10.1103/PhysRevB.43.8808 (1996).
14. Landron, C., Lefloch, S., Gervais, M., Coutures, J. P. & Bazin, D. Yttrium coordination shell in YAG related structures. *Phys. Stat. Sol (b)*. **196**, 25–31. https://doi.org/10.1002/pssb.2221960104 (1991).
15. Babin, V. Time-resolved spectroscopy of exciton States in single crystals and single crystalline films of $YAlO_3$ and $YAlO_3$: Ce. *J. Phys. D*. **44**, 315402. https://doi.org/10.1088/0022-3727/44/31/315402 (2011).
16. Kuklja, M. M. & Pandey, R. First-principles study of defect formation in yttrium aluminum Garnet. *J. Am. Ceram. Soc.* **82**, 2881–2886. https://doi.org/10.1111/j.1151-2916.1999.tb02172.x (1999).
17. Kuklja, M. M. Mechanisms of defect interactions in yttrium aluminum Garnet. *J. Phys. Condens. Matter* **12**, 2953–2968 (2000).
18. Liu, B., Gu, M., Liu, X., Huang, S. & Ni, C. Formation energies of antisite defects in $Y_3Al_5O_{12}$: A first-principles study. *Appl. Phys. Lett.* **94**, 121910. https://doi.org/10.1063/1.3109799 (2009).
19. Nikl, M., Laguta, V. V. & Vedda, A. Luminescence and defects in rare-earth doped scintillators. *Phys. Stat. Sol B*. **245**, 1701–1722. https://doi.org/10.1002/pssb.200844039 (2008).
20. Stanek, C. R., Mcclellan, K. J., Levy, M. R., Milanese, C. & Grimes, R. W. The effect of intrinsic defects on $RE_3Al_5O_{12}$ Garnet scintillator performance. *Nucl. Instrum. Meth B*. **579**, 27–30. https://doi.org/10.1016/j.nima.2007.04.006 (2007).
21. Pankratova, V., Butikova, J., Kotlov, A., Popov, A. I. & Pankratov, V. Influence of swift heavy ions irradiation on optical and luminescence properties of $Y_3Al_5O_{12}$ single crystal. *Opt. Mater. X*. **23**, 100341. https://doi.org/10.1016/j.omx.2024.100341.((2024).
22. Han, X. et al. Structural damage and recrystallization response of Garnet crystals to intense electronic excitation. *Adv. Funct. Mater.* **33**, 2212853. https://doi.org/10.1002/adfm.202212853 (2022).

23. Bhandari, K. Radiation response of $Y_3Al_5O_{12}$ and Nd^{3+}-$Y_3Al_5O_{12}$ to swift heavy ions: insight into structural damage and defect dynamics. *Phys. Chem. Chem. Phys.* **25**, 20495–20509. https://doi.org/10.1039/D3CP02734A (2023).
24. Karipbayev, Z. et al. Optical, structural, and mechanical properties of $Gd_3Ga_5O_{12}$ single crystals irradiated with $^{84}Kr^+$ ions. *Phys. Stat. Sol (b)* https://doi.org/10.1002/pssb.202100415 (2022).
25. Amekura, H., Li, R., Okubo, N., Ishikawa, N. & Chen, F. Swift heavy ion irradiation to non-amorphizable CaF_2 and amorphizable $Y_3Al_5O_{12}$ (YAG) crystals. *Nucl. Instrum. Meth B.* **474**, 78–82. https://doi.org/10.1016/j.nimb.2020.04.023 (2020).
26. Van Vuuren, A. J. et al. The influence of stopping power and temperature on latent track formation in YAP and YAG. *Nucl. Instrum. Meth B.* **460**, 67–73. https://doi.org/10.1016/j.nimb.2018.11.032 (2019).
27. Rymzhanov, R. Recrystallization as the governing mechanism of ion track formation. *Sci. Rep.* **9**, 3837. https://doi.org/10.1038/s41598-019-40239-9 (2019).
28. Izerroukenm, M., Khereddinem, A., Sarim, A. & Meftahm, A. Mechanical properties of swift heavy ion irradiated $Y_3Al_5O_{12}$ single crystal. *Nucl. Instrum. Meth B.* **435**, 137–141. https://doi.org/10.1016/j.nimb.2018.01.009 (2018).
29. Izerroukenm, M., Bucher, R., Meftah, A. & Maaza, M. XRD and AFM study of radiation damage induced by swift heavy ions in $Y_3Al_5O_{12}$ single crystals. *Radiat. Eff. Defects Solids*. **166**, 513–521. https://doi.org/10.1080/10420150.2011.559234 (2011).
30. Izerrouken, M., Meftah, A. & Nekkab, M. Radiation damage induced by swift heavy ions and reactor neutrons in $Y_3Al_5O_{12}$ single crystals. *Nucl. Instrum. Meth.* **258**, 395–402. https://doi.org/10.1016/j.nimb.2007.02.092 (2007).
31. Fleischer, R. L., Price, P. B. & Walker, R. M. *Nuclear Tracks in Solids: Principles and Application* (Univ. of California Press, 2002).
32. Komarov, F. Nano- and microstructuring of solids by swift heavy ions. *Phys. Uspekhi*. **60**, 435–471. https://doi.org/10.3367/UFNe.2016.10.038012 (2017).
33. Lushchik, A. On the mechanisms of radiation damage and prospects of their suppression in complex metal oxides. *Phys. Status Solidi B.* **250**, 261–270. https://doi.org/10.1002/pssb.201200488 (2013).
34. Vaddigiri, A., Simmons Potter, K., Thomes, W. J. & Meister, D. C. Ionizing radiation effects in Single-Crystal and polycrystalline YAG. *IEEE Trans. Nucl. Sci.* **53**, 3882–3888. https://doi.org/10.1109/TNS.2006.885951 (2006).
35. Saifulin, M. M. Latent tracks in bulk yttrium-iron Garnet crystals irradiated with low and high velocity Krypton and Xenon ions. *Nuclear Inst. Methods Phys. Res. B.* **460**, 98–103. https://doi.org/10.1016/j.nimb.2018.11.023 (2019).
36. Costantini, J. M., Miro, S., Beuneu, F. & Toulemonde, M. Swift heavy ion-beam induced amorphization and recrystallization of yttrium iron Garnet. *J. Phys. : Condens. Matter*. **27**, 496001. https://doi.org/10.1088/0953-8984/27/49/496001 (2015).
37. Costantini, J. M., Miro, S., Lelong, G., Guillaumet, M. & Toulemonde, M. Damage induced in garnets by heavy ion irradiations: a study by optical spectroscopies. *Phil. Mag.* **99**, 1695–1714. https://doi.org/10.1080/14786435.2017.1403659 (2017).
38. Ziegler, F., Ziegler, M. D. & Biersack, J. R. SRIM – The stopping and range of ions in matter. *Nucl. Instrum. Meth B.* **268**, 1818–1823. https://doi.org/10.1016/j.nimb.2010.02.091 (2010).
39. Oliver, W. C. & Pharr, G. M. An improved technique for determining hardness and elastic modulus using load and displacement sensing indentation experiments. *J. Mater. Res.* **7**, 1564–1583. https://doi.org/10.1557/JMR.1992.1564 (1992).
40. Springis, M., Pujats, A. & Valbis, J. Polarization of luminescence of colour centres in YAG crystals. *J. Phys. Condens. Matter* **3**, 5457–5462. https://doi.org/10.1088/0953-8984/3/28/021 (1991).
41. Popov, A. I., Kotomin, E. A. & Maier, J. Basic properties of the F-type centers in halides, oxides and perovskites. *Nucl. Instrum. Methods Phys. Res. B.* **268**, 3084–3089. https://doi.org/10.1016/j.nimb.2010.05.053 (2010).
42. Zorenko, Y., Zorenko, T. & Voznyak, T. Luminescence centers in $Y_3Al_5O_{12}$: La single crystals. *J. Phys. Conf. Ser.* **289**, 012028 (2011).
43. Zorenko, Y. et al. Luminescence of F^+ and F centers in AI_2O_3-Y_2O_3 oxide compounds. *IOP Conf. Ser. Mater. Sci. Eng.* **15**, 012060. https://doi.org/10.1088/1757-899X/15/1/012060 (2010).
44. Mori, K. Transient colour centres caused by UV light irradiation in yttrium aluminum Garnet crystals. *Phys. Stat. Sol (a).* **42**, 375–384. https://doi.org/10.1002/pssa.2210420142 (1977).
45. Masumoto, T. & Kuwano, Y. Effects of oxygen pressure on optical absorption of YAG. *Jpn J. Appl. Phys.* **24**, 546. https://doi.org/10.1143/JJAP.24.546 (1985).
46. Kvapil, J. & Kvapil, Josef, Perner, B. O^- centre formation in YAG crystals doped with rare Earth ions. *Cryst. Res. Technol.* https://doi.org/10.1002/crat.19750100211 (1975)., 10 161.
47. Zorenko, Y. Comparative study of the luminescence of $Y_3Al_5O_{12}$ nanoceramics and single crystals under excitation by synchrotron radiation. *Opt. Mat.* https://doi.org/10.1016/J.OPTMAT.2012.07.009 (2049).
48. Toulemonde, M., Dufour, C., Meftah, A. & Paumier, E. Transient thermal processes in heavy ion irradiation of crystalline inorganic insulators. *Nucl. Instrum. Meth B.* **166–167**, 903–912. https://doi.org/10.1016/S0168-583X(99)00799-5 (2000).
49. Wesch, W. & Wendler, E. I. Beam Modification of Solids (Eds. Wesch W. & Wendler)Springer Series in Surface Sciences, Springer International Publishing, Switzerland, (2016).
50. Lang, M. Fission tracks simulated by swift heavy ions at crustal pressures and temperatures. *Earth Planet. Sci. Lett.* **274**, 355–358. https://doi.org/10.1016/j.epsl.2008.07.039 (2008).
51. Meftah, A. Thermal Spike model applied to the irradiated yttrium iron garnet: mean diffusion length of the energy deposited on the electrons. *Nucl. Instrum. Meth B.* **122**, 470–475. https://doi.org/10.1016/S0168-583X(96)00666-0 (1997).
52. Poulos, M. Lattice dynamics and thermodynamic properties of $Y_3Al_5O_{12}$ (YAG). *J. Phys. Chem. Solids.* **162**, 110512. https://doi.org/10.1016/j.jpcs.2021.110512 (2022).
53. Kostić, Z. Ž. Study of structural and optical properties of YAG and nd:yag single crystals. *Mater. Res. Bull.* **63**, 80–87. https://doi.org/10.1016/j.materresbull.2014.11.033 (2015).
54. Papagelis, K., Kanellis, G., Arvanitidis, J., Kourouklis, G. A. & Ves, S. Phonons in rare Earth aluminum garnets and their relation to lattice vibration of AlO_4. *Phys. Status Solidi (b).* **215**, 193–198. https://doi.org/10.1002/(SICI)1521-3951(199909)215:1%3C193::AID-PSSB193%3E3.0.CO;2-G (1999).
55. Papagelis, K., Kanellis, G., Ves, S. & Kourouklis, G. A. Lattice dynamical properties of the rare Earth aluminum garnets ($RE_3Al_5O_{12}$). *Phys. Status Solidi (b).* **233**, 134–150. https://doi.org/10.1002/1521-3951(200209)233:1%3C134::AID-PSSB134%3E3.0.CO;2-Z (2002).
56. Assylbayev, R. et al. Influence of Energetic Xe^{132} Ion Irradiation on Optical, Luminescent and Structural Properties of Ce-DopedY_3Al_5O12 SingleCrystals.. *Crystals* **15**, 683. https://doi.org/10.3390/cryst1508068 (2025).

Acknowledgements

This work was supported by the Science Committee of the Ministry of Science and Higher Education of the Republic of Kazakhstan (Grant No. AP19574768).Alma Dauletbekova expresses her gratitude to the Latvian Academy of Sciences (Riga, Latvia) for its support. Yuriy Zorenko and Artur Majewski-Napierkowski are grateful for support of National Scientific Center (NCN) of Poland in frame of NCN 2022/47/I/ST8/02600 project.The authors are grateful for the support provided by DESY (Hamburg, Germany), the Institute of Solid State Physics (Riga, Latvia), and the Cyclotron DC-60 (Astana, Kazakhstan).

Author contributions

Zhakyp Dosmagambetov, Abdirash Akilbekov, Zhakyp Karipbayev, Gulnara Aralbayeva, Ilze Manika, Reinis

Ignatans, Krisjanis Smits, Artur Majewski-Napierkowski, and Yuriy Zorenko conducted the experiment and authored the original publication. Zh. Dosmagambetov, Zh. Karipbayev, Majewski-Napierkowski, R. Ignatans, G. Aralbayeva and R. Assylbayev prepared figures and Tables. A. Dauletbekova, A. Akilbekov, A. Popov, and Y. Zorenko reviewed the introduction and experimental part analysis. G. Aralbayeva and Y. Zorenkoreviewed the findings and consequences. Adhimoorthy R. Ignatans, K. Smits generated and analyzed the TEM images. The main body of the papre is written by A. Dauletbekova and Y. Zorenko. All authors reviewed and approved the final version of the text.

Funding
The Science Committee of the Ministry of Science and Higher Education of the Republic of Kazakhstan (Grant No. AP19574768).

Declarations

Competing interests
The authors declare no competing interests.

Additional information
Correspondence and requests for materials should be addressed to A.D.

Reprints and permissions information is available at www.nature.com/reprints.

Publisher's note Springer Nature remains neutral with regard to jurisdictional claims in published maps and institutional affiliations.